# Pushing and pulling optical pressure control with plasmonic surface waves

Li-Fan Yang and Kevin J. Webb*

*School of Electrical and Computer Engineering, Purdue University, West Lafayette, Indiana 47907, USA*

(Received 17 August 2020; revised 3 May 2021; accepted 26 May 2021; published 15 June 2021)

The basis for pulling a passive nanostructured material using laser light by establishing a transverse surface plasmon resonance on the back of a membrane is presented and supported with both theory and numerical simulations. The total force magnitude and direction can be regulated by electromagnetic resonant modes interacting with materials that can be adjusted using the material and geometry variables, and with plane-wave illumination under sinusoidal steady-state conditions. In the situations treated, the structured material is fixed in position and the force density and hence total force are determined numerically. Simulations indicate that a silicon nitride film coated with gold and patterned to produce a unit cell having a slot passing through both materials allows satisfactory surface wave control to facilitate a pulling force with visible wavelengths. When the plasmon surface wave on the back dominates, pulling occurs, and when the mode on the front has more energy, the result is pushing. It is also shown that pushing or pulling, regulated by varying the wavelength of the incident light, is possible, and an example is presented. This work motivates an experimental effort to investigate pulling with nanostructured media and offers a different paradigm in optomechanics.

DOI: 10.1103/PhysRevB.103.245124

## I. INTRODUCTION

While it has been more than a century since experiments have shown optical radiation can exert a mechanical pushing force on a mirror [1,2], in a manner consistent with the prediction of Maxwell [3], important basic physical questions remain and fundamentally new opportunities exist related to the mechanical action of light in material. We present a class of nanostructured material where an optical resonance is established on the back that facilitates pulling. A detailed theoretical development and numerical simulations of fields and force densities for various examples with a model that enforces momentum conservation support the concept. In the regime considered, the structure is strongly scattering, presenting a different picture to the laser tweezing work of Ashkin and others [4,5], which have led to instruments important to molecular biology [6].

A negative force can be imparted on small particles by structuring or controlling the incident beam [7–10]. More generally, field control provides a means to regulate local fields and power flow, and this can lead to the creation of vortices [11]. Small particles in a beam trap will of course be moved with and due to the trap [5]. A medium with gain can have an associated negative force [12–14]. Evanescent fields from total internal reflection or waveguide modes may produce an attractive force on another waveguide or object [15,16]. A pulling force by design of the background medium parameters has been proposed [17]. Control of effective medium parameters has also been studied in regard to negative forces [14,18]. However, a beam is generally understood to only push a mirror or planar interface or passive film. Simulation results presented indicate that both pushing and pulling can be achieved with a single normally incident plane wave on a nanostructured membrane by exciting a plasmonic mode cavity resonance on the same side (pushing) or the opposite side (pulling) of a nanostructured membrane. This is consistent with establishing a cavity resonance that has suitable asymmetry with respect to the net force direction [19] and where substantial energy is stored in the fields in the material. Excitation of such a resonant mode in the material is necessary to achieve pulling by regulating the stored energy of the resonant field as we describe.

The focus here is on metal-insulator (MI) structures that support surface plasmon modes, as presented conceptually in Fig. 1, and we consider a two-dimensional (2D) geometry. The red arrows indicate the normally incident plane wave and the gray arrows the direction of the imparted force [pushing in Fig. 1(a) and pulling in Fig. 1(b)]. If we consider the shaded region as a metal (Au is assumed in the simulations) having a dielectric constant $\epsilon = \epsilon' + i\epsilon''$, with $\epsilon' < -1$, surface (MI) waveguide modes (plasmons) can be exited on the top (front) and bottom (back) surfaces (shown as resonant field profiles outside and inside the material in Fig. 1) for transverse magnetic (TM) fields with a magnetic field perpendicular to the plane containing the arrows, assuming a free-space background. We use a coordinate system such that TM fields have $H_z$, $E_x$, $E_y$, with $H_z$ perpendicular to the plane depicted (perpendicular to the plane with the arrows in Fig. 1 and tangential to the top and bottom surfaces). The slot has a lowest-order [metal-insulator-metal (MIM)] mode (having $H_z, E_x, E_y$) that propagates for arbitrarily small slot width and can provide for resonant coupling through the film [20–22]. A normally incident plane wave from the top ($H_z, E_x$) excites the slot mode and hence the front and back surface waves to some extent. The evanescent nature of the surface wave confines the field to the metal interface, and, collectively with the resonant condition, substantial field energy is stored near the

*Corresponding author: webb@purdue.edu

 

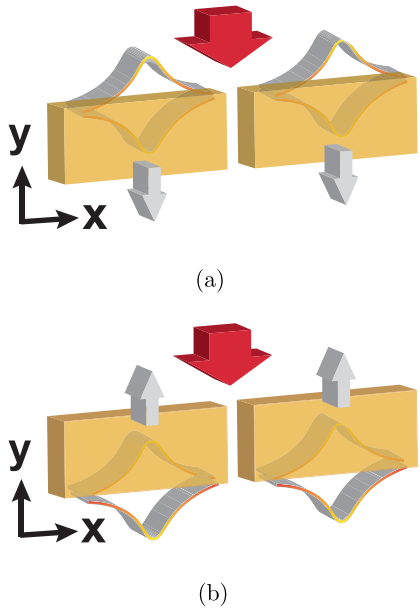


FIG. 1. Illustration of pushing (a) and pulling (b) of structures, relative to the direction of the incident light (red arrow) and associated with the excitation of resonant plasmon surface waves. The gray arrows indicate the force direction experienced by the material. In the pushing case in (a), the dominant surface wave is on the top or incident beam side, and for the pulling situation in (b), the dominant transversely resonant plasmon mode is on the back (bottom). A transversely periodic structure is considered, and one period is shown. Periodic boundary conditions are thus imposed on the left and the right. All geometries involve a slot passing through the structure that support a metal-insulator-metal waveguide mode that can provide resonant coupling through the film as well as scatter-based excitation of the transverse surface (metal-insulator) mode.

surface and in the material. With a slot cavity resonance in the longitudinal dimension (the $y$ direction, where the red arrows in Fig. 1 are in the $-y$ direction), coupling through the film and excitation of the back surface wave is promoted. Adding a dielectric layer to the top or bottom surface and adjustment of the geometry allows either the front [pushing, Fig. 1(a)] or back [pulling, Fig. 1(b)] to have a large, transversely resonant surface wave. A surface wave on the top results in a pushing force (from the force density in the material), indicated by the gray arrows in Fig. 1(a), and on the bottom a pulling force, where there is pushing from the back of the material (associated with the force density in the material in that region), as illustrated by the gray arrows in Fig. 1(b). Surface waves on a (lossy) metal have a normal Poynting vector component and force into the metal, and these can be large with resonance relative to the contributions from the relatively small incident photon flux. On this basis, pulling, as in Fig. 1(b), is presented through simulations with a model based on the work of Einstein and Laub that enforces conservation of momentum [23].

The force theory in various forms used in the simulations is summarized in Sec. II. The relevant boundary physics is reviewed in Sec. III, and this motivates the more detailed derivation of the force density and momentum conservation conditions at boundaries in Sec. IV. This leads to important conclusions regarding the treatment of forces in materials due to electromagnetic fields. Section V presents simulation results for pushing and pulling forces in nanostructured metal-dielectric films, and Sec. VI provides a discussion of various calculations of pulling forces in this situation and more general perspectives of force and energy in coherent resonant systems. The work and related impact are summarized in Sec. VII.

## II. FORCE THEORY FOR SIMULATIONS

We describe the force theory that is used to generate the simulation results. The approach uses the fields in the material to describe the optical force density, and is based on the work of Einstein and Laub [23], which gives

$$\mathbf{f} = \frac{\partial \mathbf{P}}{\partial t} \times \mu_0 \mathbf{H} - \frac{\partial \mu_0 \mathbf{M}}{\partial t} \times \epsilon_0 \mathbf{E} + \rho \mathbf{E} + \mathbf{J} \times \mu_0 \mathbf{H} + (\mathbf{P} \cdot \nabla)\mathbf{E} + \mu_0 (\mathbf{M} \cdot \nabla)\mathbf{H}, \tag{1}$$

with $\mathbf{f}$ having SI units of N/m$^3$ and $\mathbf{P}$ the polarization, $\mathbf{H}$ the magnetic field intensity, $\mathbf{M}$ the magnetization, $\mathbf{E}$ the electric field intensity, $\rho$ the electric charge density, $\mathbf{J}$ the electric current density, $\mu_0$ the permeability of free space, and $\epsilon_0$ the permittivity of free space [24–26]. The kinetic force density in (1) is obtained from

$$\mathbf{f} = -\left(\nabla \cdot \mathbf{T} + \frac{\partial \mathbf{g}}{\partial t}\right), \tag{2}$$

with $\mathbf{g}$ the momentum density and where $\mathbf{T}$ is the associated Einstein-Laub stress tensor, given by [25]

$$\mathbf{T} = \tfrac{1}{2}(\epsilon_0 \mathbf{E} \cdot \mathbf{E} + \mu_0 \mathbf{H} \cdot \mathbf{H})\mathbf{I} - \mathbf{DE} - \mathbf{BH}, \tag{3}$$

with $\mathbf{I}$ the identity matrix, $\mathbf{D}$ the electric flux density, $\mathbf{B}$ the magnetic flux density, and where $\mathbf{DE}$ and $\mathbf{BH}$ indicate the relevant tensors, for example,

$$\mathbf{DE} = \begin{bmatrix} D_1E_1 & D_1E_2 & D_1E_3 \\ D_2E_1 & D_2E_2 & D_2E_3 \\ D_3E_1 & D_3E_2 & D_3E_3 \end{bmatrix}. \tag{4}$$

The divergence of the tensor in the $(x_1, x_2, x_3)$ coordinate system is

$$\nabla \cdot \mathbf{T} = \begin{bmatrix} \frac{\partial T_{11}}{\partial x_1} + \frac{\partial T_{21}}{\partial x_2} + \frac{\partial T_{31}}{\partial x_3} \\ \frac{\partial T_{12}}{\partial x_1} + \frac{\partial T_{22}}{\partial x_2} + \frac{\partial T_{32}}{\partial x_3} \\ \frac{\partial T_{13}}{\partial x_1} + \frac{\partial T_{23}}{\partial x_2} + \frac{\partial T_{33}}{\partial x_3} \end{bmatrix}. \tag{5}$$

Equation (1) assumes the Abraham momentum, which leads to

$$\mathbf{g} = \frac{1}{c^2}\mathbf{E} \times \mathbf{H}, \tag{6}$$

with $c$ the speed of light in vacuum. For electromagnetic energy in free space, this yields the single-photon momentum magnitude of $\hbar k_0$, where $\hbar = h/2\pi$, with $h$ being Planck's constant, and $k_0$ is the free-space wave number.

Equation (1) has been used to describe key experiments [24,25], notably the bulge on a liquid surface due to a laser [4], and results in the theory of Lorentz in the static limit [26]. Some important conclusions related to the interpretation of (2), in regards to metal-dielectric boundaries that support surface plasmon waves, are pursued in Sec. IV.

We assume a time-harmonic, monochromatic field description with frequency dependence $\exp(-i\omega t)$, along with an isotropic dielectric response, giving $\mathbf{P}(\mathbf{r},\omega) = \epsilon_0\chi_E(\mathbf{r},\omega)\mathbf{E}(\mathbf{r},\omega)$, with $\chi_E$ the complex electric susceptibility (leading to a complex dielectric constant $\epsilon = 1+\chi_E$). The time average of the force density in the frequency domain and in source-free dielectric media, from (1), can be thus written as [27]

$$\langle \mathbf{f}\rangle = \frac{\omega\mu_0}{2}\mathrm{Im}\{\mathbf{P}\times\mathbf{H}^*\} + \frac{1}{2}\mathrm{Re}\{(\mathbf{P}\cdot\nabla)\mathbf{E}^*\}, \tag{7}$$

where $\langle\cdot\rangle$ is the temporal average, $\mathrm{Re}\{\cdot\}$ is the real part, and $\mathrm{Im}\{\cdot\}$ is the imaginary part, and $\mathbf{P}$, $\mathbf{E}$, and $\mathbf{H}$ are phasors. Equation (7) is used to obtain the force density in the material, integrated to form the force, and normalized by the periodic geometry to form pressure.

Assuming a 2D transversely periodic arrangement with fields $H_z(x,y)$, $E_x(x,y)$, $E_y(x,y)$ and interest in the $y$ component of the force (so the $x$ direction has a periodic boundary condition with no net total force in that direction), the first term in (7) yields

$$\frac{\omega\mu_0}{2}\mathrm{Im}\{\hat{\mathbf{y}}\cdot(\mathbf{P}\times\mathbf{H}^*)\} = \frac{\omega\mu_0\epsilon_0}{2}\mathrm{Im}\{\chi_E(E_zH_x^* - E_xH_z^*)\}. \tag{8}$$

For the second term in (7),

$$(\mathbf{P}\cdot\nabla)\mathbf{E}^* = \begin{bmatrix} P_x\frac{\partial E_x^*}{\partial x} + P_y\frac{\partial E_x^*}{\partial y} + P_z\frac{\partial E_x^*}{\partial z} \\ P_x\frac{\partial E_y^*}{\partial x} + P_y\frac{\partial E_y^*}{\partial y} + P_z\frac{\partial E_y^*}{\partial z} \\ P_x\frac{\partial E_z^*}{\partial x} + P_y\frac{\partial E_z^*}{\partial y} + P_z\frac{\partial E_z^*}{\partial z} \end{bmatrix}. \tag{9}$$

In 2D, this leads to

$$\frac{1}{2}\Re\{\hat{\mathbf{y}}\cdot(\mathbf{P}\cdot\nabla)\mathbf{E}^*\} = \frac{\epsilon_0}{2}\mathrm{Re}\left\{\chi_E\left(E_x\frac{\partial E_y^*}{\partial x} + E_y\frac{\partial E_y^*}{\partial y} + E_z\frac{\partial E_y^*}{\partial z}\right)\right\}. \tag{10}$$

Equation (7) is implemented as (8) and (10) to form the $y$ component (normal to the top surface in Fig. 1) of the force density throughout the material as

$$\langle f_y(x,y)\rangle = \frac{\omega\mu_0\epsilon_0}{2}\mathrm{Im}\{\chi_E(E_zH_x^* - E_xH_z^*)\} + \frac{\epsilon_0}{2}\mathrm{Re}\left\{\chi_E\left(E_x\frac{\partial E_y^*}{\partial x} + E_y\frac{\partial E_y^*}{\partial y} + E_z\frac{\partial E_y^*}{\partial z}\right)\right\}. \tag{11}$$

Equation (11) is integrated (over one period in the transverse direction) to form the $y$-directed, or normal, total force, and then divided by the relevant transverse dimensions (the period and unit distance in the space-invariant $z$ direction) to obtain the pressure.

For monochromatic radiation (single $\omega$), it can be shown that $\langle\partial\mathbf{g}/\partial t\rangle = 0$ (see the Appendix for a proof). Consequently, the time-average force density in the material is, from (2),

$$\langle\mathbf{f}\rangle = -\langle\nabla\cdot\mathbf{T}\rangle. \tag{12}$$

From (12), for sinusoidal steady-state conditions, the force density in the material is equivalently available from the divergence of the stress tensor. The divergence of $\mathbf{T}$ is formed as (5), and, for example, the divergence of (4) is

$$\nabla\cdot\mathbf{DE} = \begin{bmatrix} \frac{\partial(D_xE_x)}{\partial x} + \frac{\partial(D_xE_y)}{\partial y} + \frac{\partial(D_xE_z)}{\partial z} \\ \frac{\partial(D_yE_x)}{\partial x} + \frac{\partial(D_yE_y)}{\partial y} + \frac{\partial(D_yE_z)}{\partial z} \\ \frac{\partial(D_zE_x)}{\partial x} + \frac{\partial(D_zE_y)}{\partial y} + \frac{\partial(D_zE_z)}{\partial z} \end{bmatrix}. \tag{13}$$

Assuming locally homogeneous media, we have

$$\nabla\cdot\mathbf{DE} = \nabla\cdot[(\epsilon_0\mathbf{E} + \epsilon_0\chi_E\mathbf{E})\mathbf{E}] \tag{14}$$

$$= \epsilon_0(1+\chi_E)\nabla\cdot\mathbf{EE}, \tag{15}$$

where we imply piecewise constant $\chi_E$, as occurs in numerical solutions with subdomain basis functions, such as in the finite-element method (FEM) solution of electromagnetic problems. The relevant component of the time average of the divergence of (12) thus becomes

$$\begin{aligned}\langle f_y(x,y)\rangle &= -\frac{1}{2}\mathrm{Re}\{\langle\hat{\mathbf{y}}\cdot(\nabla\cdot\mathbf{T})\rangle\} \\ &= -\frac{1}{2}\mathrm{Re}\left\{\frac{\partial}{\partial y}\left[\frac{\epsilon_0}{2}\left(|E_x|^2 + |E_y|^2\right) + \frac{\mu_0}{2}|H_z|^2\right]\right. \\ &\quad \left. -\epsilon_0(1+\chi_E)\left[\frac{\partial\left(E_xE_y^*\right)}{\partial x} + \frac{\partial(|E_y|^2)}{\partial y}\right]\right\}.\end{aligned} \tag{16}$$

Equation (16) is implemented numerically.

Application of the divergence theorem to the stress tensor with elements $T_{ij}$ for the coordinate system $(x_1,x_2,x_3)$ results in

$$\int\left(\frac{\partial T_{i1}}{\partial x_1} + \frac{\partial T_{i2}}{\partial x_2} + \frac{\partial T_{i3}}{\partial x_3}\right)dv = \oint T_{i1}ds_1 + T_{i2}ds_2 + T_{i3}ds_3, \tag{17}$$

for $i = 1,2,3$. When the surface integral spans a material interface and contracts to that surface, the closed surface integral is zero only when the $T_{ij}$ are continuous across the relevant boundary. For TM-polarized fields $(H_z,E_x,E_y)$, the discontinuity in the normal electric fields at interfaces results in a discontinuity in the associated terms of $\mathbf{T}$. With $(x_1,x_2,x_3)\to(x,y,z)$, time-harmonic fields, the stress tensor in (3), and assuming $H_z(x,y)$, $E_x(x,y)$, $E_y(x,y)$, the time-averaged stress tensor elements are given by

$$\langle T_{yx}\rangle = -\tfrac{1}{2}\mathrm{Re}\{D_yE_x^*\}, \tag{18}$$

$$\langle T_{yy}\rangle = \frac{\epsilon_0}{4}\mathrm{Re}\{\mathbf{E}\cdot\mathbf{E}^*\} + \frac{\mu_0}{4}\mathrm{Re}\{\mathbf{H}\cdot\mathbf{H}^*\} - \frac{1}{2}\mathrm{Re}\{D_yE_y^*\}, \tag{19}$$

$$\langle T_{yz}\rangle = 0. \tag{20}$$

Application of the divergence theorem to the stress tensor in (3) yields the $y$ component of the total time-averaged force (over one period and unit distance in the space-invariant direction) as

$$\langle F_y\rangle = \oint\langle T_{yx}\rangle dy\,dz + \langle T_{yy}\rangle dx\,dz, \tag{21}$$

where, consistent with (17), an outward normal unit-vector direction is assumed for each surface, and the $\hat{\mathbf{z}}$ components

of the closed surface integrals are zero in the 2D situation considered. Equation (21) can thus be used to also determine the force on a particular region of material.

We present numerical results for the pressure (pushing and pulling) for structures like Fig. 1 using (11), (16), and (21). However, first the boundary conditions for the metal are considered physically (Sec. III) and mathematically (Sec. IV). We note the significance of these steps in relation to the integration of the force density within the spatial support of the material and access to field resonances in the material to regulate the force.

## III. PLASMONIC SURFACE WAVES AND BOUNDARY CONDITIONS

A set of experiments measuring the deflection of a nanostructured Au-SiN membrane supporting resonant plasmon surface waves due to an incident laser beam concluded that a pressure greater than that on a perfect mirror is possible [27]. The physical understanding is that this is due to an asymmetric cavity resonance and the energy associated with a large number of photons in the material [19]. Adjustment of the conditions for the plasmon surface wave resonance are shown to allow for pulling.

Maxwell's picture [1–3] gives a pressure

$$P = \frac{S}{c}(1 + |\Gamma|^2), \tag{22}$$

where $S$ is the time-average incident Poynting vector magnitude and $\Gamma$ is the field reflection coefficient, and no transmission through the material is implied. The maximum pressure from (22) is $2S/c$. Experimental evidence indicates that this value was exceeded by utilizing structured material in the third dimension and from surface plasmon resonances [27]. Equation (7) is the force density model used to predict the measured data with tight error tolerances. This model is used here to investigate pulling forces, under the assumption that earlier experiments support this position. However, there remain open issues related to optical forces at interfaces that suggest further experiments are in order.

Interesting aspects of field boundary conditions at material interfaces have been noted [28]. We consider the physics of metal-insulator interfaces, as is relevant for forces on nanostructured membranes supporting plasmon surface waves. In general, the treatment of electromagnetics and optical force density at nanometer length scales and in nanostructured material requires consideration of nonlocal effects in both time and space [29]. Metal [30] and semiconductor [31] interfaces have been studied based on (Thomas-Fermi) screening, where electrons screen the electric field from the positively charged relatively immobile atoms, leading to wave-vector-dependent and spatially dependent dielectric functions. These nonlocal effects have been modeled simply as a modification of the Drude picture, and an equivalent boundary-layer representation has been chosen to use local dielectric functions [32]. In application of a hydrodynamic representation (see, for example, [33]), continuity of the normal component of the electric field across the vacuum-metal interface was sought [34,35], with the normal polarization going to zero. Such microscopic models apply to length scales comparable to the (de Broglie) wavelength in the metal, 0.5 nm or so, and describe the shortcomings of a sheet charge supporting a step discontinuity in the normal electric field at the vacuum-metal interface, and the fact that the electrons are distributed (and screen the positive charges). This body of work may indicate that there is no boundary force from the Dirac function associated with the second term in (7) and the discontinuity of the normal component of the electric field at a metal-vacuum interface. This, and hence the integration of (7) within the metal and not across the boundary, was previously assumed [36] and used to predict experimental results [27].

One might consider an atomistic treatment of the material, considering it as a set of voxels (pixels in 2D), which is equivalent to the model presented by Gordon [37] and consistent with a picture from Shockley [38,39]. This interpretation involves applying (7) at the atomic scale, where the dipole moment for each atom, $\mathbf{p}$, has a force according to the local fields (called the Lorentz force in [37]), but with the form in (7). In this case, each pixel acts much like an atom. If one varies the local dipole moment of one of these atoms, the resulting force (Born approximation for the perturbation) would use the background field. Each voxel and each atom would conform to this picture. In 2D, thin sheets of material (metal) have image charges and do not experience a force in slowly varying background fields, and it is the long-range variation that would regulate the evolving force density. This description leads to a bulk interpretation of (7) without boundary contributions on each element.

Recent experimental work related to photon drag at a metal surface has raised important questions about our understanding of optical forces at such interfaces [40]. Surface waves at metal interfaces provide an interesting situation with regard to optical forces. It is thus clear that more experimental work is needed to resolve the underlying physics. As will be described here based on simulations, it may be possible to pull a structure, and in fact to push or pull depending on the conditions of the incident light. Section IV considers the mathematical development of the optical force density in materials more completely, notably, in relation to the boundary conditions at metal-insulator surfaces.

## IV. FORCE THEORY AND BOUNDARY CONDITIONS

We pursue a detailed development of the force density in (1) and the resulting total force that provides a basis for considering the implications of field boundary conditions. This establishes the conservation of momentum imposed pointwise using (1) and enables important new conclusions about conservation of photon momentum at material boundaries, supporting use of a force density model within the material described in Sec. III. For completeness, we start with Maxwell's equations and work through the vector calculus to arrive at a basic understanding of the influence of boundaries and aspects of interpretation of a statement of momentum conservation.

Maxwell's equations, with all source terms on the right-hand side, can be written as

$$\nabla \times \mathbf{E} + \mu_0 \frac{\partial \mathbf{H}}{\partial t} = -\mu_0 \frac{\partial \mathbf{M}}{\partial t}, \tag{23}$$

$$\nabla \times \mathbf{H} - \epsilon_0 \frac{\partial \mathbf{E}}{\partial t} = \frac{\partial \mathbf{P}}{\partial t} + \mathbf{J}, \tag{24}$$

$$\epsilon_0 \nabla \cdot \mathbf{E} = -\nabla \cdot \mathbf{P} + \rho, \tag{25}$$

$$\nabla \cdot \mathbf{H} = -\nabla \cdot \mathbf{M}, \tag{26}$$

where all quantities have been defined in relation to (1). Note that material dispersion and loss are incorporated into the polarization and magnetization through the frequency domain representation for those quantities. Taking the cross product of $\epsilon_0\mathbf{E}$ with (23) and $\mu_0\mathbf{H}$ with (24), and adding the resulting equations, gives

$$\epsilon_0 \mathbf{E} \times (\nabla \times \mathbf{E}) + \mu_0 \mathbf{H} \times (\nabla \times \mathbf{H}) + \mu_0 \epsilon_0 \mathbf{E} \times \frac{\partial \mathbf{H}}{\partial t} - \mu_0 \epsilon_0 \mathbf{H} \times \frac{\partial \mathbf{E}}{\partial t} = \mu_0 \mathbf{H} \times \frac{\partial \mathbf{P}}{\partial t} - \mu_0 \epsilon_0 \mathbf{E} \times \frac{\partial \mathbf{M}}{\partial t} + \mu_0 \mathbf{H} \times \mathbf{J}. \tag{27}$$

Using the Abraham momentum defined in (6), (27) becomes

$$\epsilon_0 \mathbf{E} \times (\nabla \times \mathbf{E}) + \mu_0 \mathbf{H} \times (\nabla \times \mathbf{H}) + \frac{\partial \mathbf{g}}{\partial t} = \mu_0 \mathbf{H} \times \frac{\partial \mathbf{P}}{\partial t} - \mu_0 \epsilon_0 \mathbf{E} \times \frac{\partial \mathbf{M}}{\partial t} + \mu_0 \mathbf{H} \times \mathbf{J}. \tag{28}$$

We apply the identity

$$(\nabla \mathbf{A}) \cdot \mathbf{B} = (\mathbf{B} \cdot \nabla)\mathbf{A} + \mathbf{B} \times (\nabla \times \mathbf{A}), \tag{29}$$

with $\mathbf{A} = \mathbf{B} = \mathbf{E}$, to write

$$\epsilon_0 \mathbf{E} \times (\nabla \times \mathbf{E}) = \tfrac{1}{2}\epsilon_0 \nabla \cdot (|\mathbf{E}|^2 \mathbf{I}) - \epsilon_0 (\mathbf{E} \cdot \nabla)\mathbf{E}, \tag{30}$$

where

$$\nabla \mathbf{E} \cdot \mathbf{E} = \frac{1}{2} \begin{bmatrix} \frac{\partial |\mathbf{E}|^2}{\partial x} \\ \frac{\partial |\mathbf{E}|^2}{\partial y} \\ \frac{\partial |\mathbf{E}|^2}{\partial z} \end{bmatrix} = \frac{1}{2} \nabla \cdot (|\mathbf{E}|^2 \mathbf{I}). \tag{31}$$

With the identity

$$(\mathbf{E} \cdot \nabla)\mathbf{E} = \nabla \cdot (\mathbf{E}\mathbf{E}) - \mathbf{E}(\nabla \cdot \mathbf{E}), \tag{32}$$

(30) becomes

$$\epsilon_0 \mathbf{E} \times (\nabla \times \mathbf{E}) = \tfrac{1}{2}\epsilon_0 \nabla \cdot (|\mathbf{E}|^2 \mathbf{I}) - \epsilon_0 \nabla \cdot (\mathbf{E}\mathbf{E}) + \epsilon_0 \mathbf{E}(\nabla \cdot \mathbf{E}). \tag{33}$$

Following a similar procedure for $\mathbf{H}$ results in

$$\epsilon_0 \mathbf{E} \times (\nabla \times \mathbf{E}) + \mu_0 \mathbf{H} \times (\nabla \times \mathbf{H}) = \nabla \cdot \mathbf{T}_E + \epsilon_0 \mathbf{E}(\nabla \cdot \mathbf{E}) + \mu_0 \mathbf{H}(\nabla \cdot \mathbf{H}), \tag{34}$$

with the momentum-flow or stress tensor for the electromagnetic field given by

$$\mathbf{T}_E = \tfrac{1}{2}(\epsilon_0 E^2 + \mu_0 H^2)\mathbf{I} - \epsilon_0 \mathbf{E}\mathbf{E} - \mu_0 \mathbf{H}\mathbf{H}. \tag{35}$$

With complete generality, we can thus write (28) as

$$\nabla \cdot \mathbf{T}_E + \frac{\partial \mathbf{g}}{\partial t} = \mu_0 \mathbf{H} \times \frac{\partial \mathbf{P}}{\partial t} - \mu_0 \epsilon_0 \mathbf{E} \times \frac{\partial \mathbf{M}}{\partial t} + \mu_0 \mathbf{H} \times \mathbf{J} - \epsilon_0 \mathbf{E}(\nabla \cdot \mathbf{E}) - \mu_0 \mathbf{H}(\nabla \cdot \mathbf{H}). \tag{36}$$

Incorporating the local forces due to $\mathbf{P}$ and $\mathbf{M}$ into (36) and making use of the identities

$$-(\nabla \cdot \mathbf{P})\mathbf{E} = -\nabla \cdot (\mathbf{P}\mathbf{E}) + (\mathbf{P} \cdot \nabla)\mathbf{E}, \tag{37}$$

$$-(\nabla \cdot \mathbf{M})\mathbf{H} = -\nabla \cdot (\mathbf{M}\mathbf{H}) + (\mathbf{M} \cdot \nabla)\mathbf{H}, \tag{38}$$

leads to

$$\nabla \cdot \mathbf{T} + \frac{\partial \mathbf{g}}{\partial t} = \mu_0 \mathbf{H} \times \frac{\partial \mathbf{P}}{\partial t} - \mu_0 \epsilon_0 \mathbf{E} \times \frac{\partial \mathbf{M}}{\partial t} + \mu_0 \mathbf{H} \times \mathbf{J} - \epsilon_0 \mathbf{E}(\nabla \cdot \mathbf{E}) - \mu_0 \mathbf{H}(\nabla \cdot \mathbf{H}) - \mathbf{E}(\nabla \cdot \mathbf{P}) - \mu_0 \mathbf{M}(\nabla \cdot \mathbf{H}) - (\mathbf{P} \cdot \nabla)\mathbf{E} - (\mathbf{M} \cdot \nabla)\mathbf{H}, \tag{39}$$

with $\mathbf{T}$ the Einstein-Laub stress tensor given by (3), formed as

$$\mathbf{T} = \mathbf{T}_E + \mathbf{P}\mathbf{E} + \mathbf{M}\mathbf{H}, \tag{40}$$

with $\mathbf{T}_E$ from (35). Substituting

$$\mathbf{D} = \epsilon_0 \mathbf{E} + \mathbf{P}, \tag{41}$$

$$\mathbf{B} = \mu_0 (\mathbf{H} + \mathbf{M}) \tag{42}$$

into (39), we have

$$\nabla \cdot \mathbf{T} + \frac{\partial \mathbf{g}}{\partial t} = \mu_0 \mathbf{H} \times \frac{\partial \mathbf{P}}{\partial t} - \mu_0 \epsilon_0 \mathbf{E} \times \frac{\partial \mathbf{M}}{\partial t} + \mu_0 \mathbf{H} \times \mathbf{J} - \rho \mathbf{E} - (\mathbf{P} \cdot \nabla)\mathbf{E} - (\mathbf{M} \cdot \nabla)\mathbf{H}. \tag{43}$$

Equation (43) provides a statement of momentum conservation at each point in space and at each instant of time. We consider now momentum conservation in the integral sense.

The point of deriving (43) and hence (1) from basic principles is to consider the implications with regard to conservation of momentum at interfaces. From (43), we have

$$\frac{\partial \mathbf{g}}{\partial t} = -\nabla \cdot \mathbf{T} - \left[ \frac{\partial \mathbf{P}}{\partial t} \times \mu_0 \mathbf{H} - \frac{\partial \mu_0 \mathbf{M}}{\partial t} \times \epsilon_0 \mathbf{E} + \mathbf{J} \times \mu_0 \mathbf{H} + \rho \mathbf{E} + (\mathbf{P} \cdot \nabla)\mathbf{E} + (\mathbf{M} \cdot \nabla)\mathbf{H} \right]. \tag{44}$$

Simplifying (44) for nonmagnetic, source-free regions,

$$\frac{\partial \mathbf{g}}{\partial t} = -\nabla \cdot \mathbf{T} - \left[ \frac{\partial \mathbf{P}}{\partial t} \times \mu_0 \mathbf{H} + (\mathbf{P} \cdot \nabla)\mathbf{E} \right]. \tag{45}$$

Integrating (45) and applying the divergence theorem results in

$$\int_v \int_t \frac{\partial \mathbf{g}}{\partial t} dv\, dt = -\oint \int_t T_{ij} ds_k dt - \int_v \int_t \left[ \frac{\partial \mathbf{P}}{\partial t} \times \mu_0 \mathbf{H} + (\mathbf{P} \cdot \nabla)\mathbf{E} \right] dv\, dt, \tag{46}$$

where the appropriate permutations of the surface integral variables are implied. The right-hand side of (46) contains a surface integral of the stress (momentum-flow) tensor and a volume integral of the force density. Conservation of momentum in the context of (46) implies that the left equals the right. We will consider (46), with an emphasis on the boundary between two materials, notably between free space and a metal, where the normal component of the electric field is discontinuous across the boundary (and hence a surface plasmon wave can be supported).

In (45) and (46), all fields are continuous across dielectric boundaries except for the normal component of the electric field, and for those fields, Gauss's law leads to the boundary conditions

$$\hat{\mathbf{n}}_{21} \cdot (\mathbf{D}_1 - \mathbf{D}_2) = \rho = 0, \tag{47}$$

$$\hat{\mathbf{n}}_{21} \cdot (\mathbf{P}_1 - \mathbf{P}_2) = \rho_{ps}, \tag{48}$$

where $\rho_{ps}$ is the polarization surface charge density at the interface, and complex $\epsilon_i$ and $\chi_{Ei}$, $i = 1, 2$, are implied. The electric field boundary condition can be obtained by setting $\mathbf{P}_i = \epsilon_0 \chi_E \mathbf{E}_i$, and the Dirac function weight for spatial derivatives follows from (48). In 2D and for the transverse electric (TE) case ($E_z, H_x, H_y$), all fields are continuous. However, for TM fields ($H_z, E_x, E_y$ that excite surface plasmon modes), there is a step in the normal component of the electric field ($E_y$) across an interface. This discontinuity of the normal electric field at an interface has interesting consequences in relation to (46).

To investigate the conservation condition across a boundary, we focus on the form in (46) as the spatial support of the integrals contract to a locally planar boundary but span that interface. The Abraham momentum is represented in the integral on the left in (46). Consequently, the integral on the left must be zero, a recognized statement of the conservation of photon momentum in the classical field sense. We consider a vacuum-metal interface, with the integrals approaching the boundary from either side ($0^-$ and $0^+$). A discontinuous normal electric field at the metal-vacuum boundary results in a discontinuous $T_{yy}$ (assuming a boundary at $y = 0$). This nonzero result for the closed surface integral as it contracts to the interface is precisely compensated by the Dirac term associated with $(\mathbf{P} \cdot \nabla)\mathbf{E}$, so that the sum of the two integrals on the right of (46) approaches zero. The discontinuous normal electric field in the cross-product term has zero contribution to the normal ($y$-directed) force density across the boundary, so it is only $(\mathbf{P} \cdot \nabla)\mathbf{E}$ that provides the compensation for a discontinuous $T_{yy}$. Within the conservation condition in (46), there is thus the question of how to apply the boundary condition in a physically meaningful manner. Because there are two terms on the right of (46), precisely how to treat each to accomplish this is worthy of consideration.

In the TM field case, we have mathematical choices for the interpretation of the two integrals on the right of (46). These are termed options that strictly enforce the conservative properties indicated in (46), but in reality, the physics (see Sec. III) and experimental results must dictate the selection. At this point, relevant experimental information is lacking.

*Option (i).* The Dirac boundary term from the volume integral [due to $(\mathbf{P} \cdot \nabla)\mathbf{E}$ across the interface] is added to the closed surface integral of the momentum-flow (stress) tensor, a step that is equivalent to adding a $T_{yy}$ boundary term that removes the step discontinuity in $T_{yy}$. This results in $T_{yy}$ being effectively continuous across the interface. Even in the perfect mirror case, continuity of $T_{yy}$ across a planar interface can be used in the limit that the skin depth approaches zero. This means that the volume integral of the force density is performed only within the material and not across the boundary interface. The continuity of the stress tensor elements is widely seen as a measure of conservation of momentum and hence a requirement [41–44]. This is consistent with the tensor describing the rate of flow of momentum [45] or energy [46] and hence needing to be a continuous variable or a conserved quantity, as presented by Schwinger [47]. In this physical situation, there is no time-average force on the differential surface layer as the thickness of that layer approaches zero. Such local momentum flux conservation is inherent in the general application of the electromagnetic stress tensor in typical classical field situations [48]. With this option, integration of the force density within the material gives the same result as the integral of the divergence of the stress tensor, through the divergence theorem, with the Dirac contribution, so the integral of the stress tensor within and around the material boundary is consistent and identical to that from the volume density. This happens because the step discontinuity in $T_{yy}$ is removed or compensated by the Dirac contribution from the term $(\mathbf{P} \cdot \nabla)\mathbf{E}$ in force density. With this interpretation, both integrals on the right of (46) yield the same total force, and momentum flow across the boundary is preserved. This approach is consistent with integration applied in the quantum regime [49] and was used to describe measurements of structured membrane deflection when plasmon modes are supported [27].

*Option (ii).* The potential step in $T_{yy}$ at the boundary is retained, so that the closed surface integral of the stress tensor across the boundary is nonzero. Consequently, a Dirac boundary term is retained in the force density. While this is difficult to implement numerically, application of the divergence theorem with a discontinuous $T_{yy}$ leads to the force from a closed surface integral external to the material. Ascribing the total force to each term in (46) yields a different force result to option (i), except for situations where $T_{yy}$ is continuous. A physical force is thus attributed to the infinitesimal boundary layer. While this may not be consistent with the microscopic physics (Sec. III), the force on this boundary layer and associated with the induced surface charge has been described previously [39] and also used when considering waves obliquely incident on a mirror [50]. An experiment to determine this Dirac boundary force has yet to be done, although this relates to the findings of Jones and Leslie [51].

*Option (iii).* Some portion of the weight of the Dirac term [from $(\mathbf{P} \cdot \nabla)\mathbf{E}$] is added to the surface integral term, leaving a contribution remaining in the volume integral. This case is a weighted form of options (i) and (ii), and may be interesting, depending on the surface physics determined from experiments in these situations.

Related to the discussion in Sec. III, there is evidently interesting and unknown physics to explore involving optical

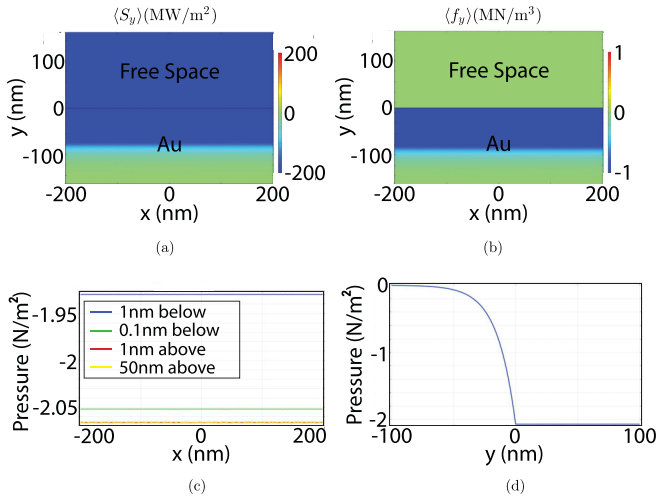


FIG. 2. Pressure on a planar vacuum-Au interface with a normally incident plane wave from the top having a free-space wavelength of 633 nm and an intensity (time-average power density) equivalent to 1 mW over 1-$\mu$m radius circle. A dielectric constant of $\epsilon_{\mathrm{Au}} = -11.8 + i1.23$ is assumed. (a) Time-average $y$-directed Poynting vector as a function of position into a planar Au surface, which is at $y = 0$. (b) Time-average $y$-directed force density ($\langle f_y \rangle$) in Au. The integrated force gives a pressure on Au with a magnitude that is just a little less ($-2.08$ N/m$^2$) than the perfect mirror result of $-2.12$ N/m$^2$ ($2S/c$). (c) The stress tensor elements $\langle T_{yy}(x) \rangle$ along various surfaces. The legend indicates the vertical position in relation to the Au surface. (d) Calculated $\langle T_{yy}(x = 0, y) \rangle$ from $y = -100$ to 100 nm.

forces at surfaces that remains to be addressed experimentally. We will assume option (i) in simulations because it is consistent with the microscopic physics discussed in Sec. III and general understanding of conservations principles, and with prior experiments [27]. Importantly, doing so opens opportunities for accessing internal material field resonances. Our position is to present simulations based on this description and allow future experiments to dictate the ultimate physical situation. The effective forced continuity of $T_{yy}$ means that the net contribution from a continuous stress tensor across the interface, which is consistent with an established picture (where the stress tensor external to the structure can be integrated) [48], will also yield the same result, i.e., this allows the external stress tensor integral to provide the same force as integration of the force density inside the material (and without the Dirac boundary term). We should note, however, that the surface screening at the vacuum-metal interface described in Sec. III might result in the situation where, even for TM fields, both the integrals across the boundary on the right of (46) are zero.

## V. RESULTS

We first present the reference case of the pressure on a planar Au surface in vacuum, determined using the theory from Sec. II. Figure 2 shows numerical force density and pressure simulations for a Au film that is sufficiently thick at 200 nm to be considered semi-infinite. A 633-nm plane wave is normally incident from the top ($H_z$, $E_x$). For Au, a dielectric constant of $\epsilon_{\mathrm{Au}} = -11.8 + i1.23$ is assumed [52]. The diminishing time-average Poynting vector into the metal in Fig. 2(a) is consistent with the force density calculation using (7) and shown in Fig. 2(b). Applying the divergence theorem to the stress tensor in (3), the relevant tensor component ($\langle T_{yy} \rangle$) from (19) is plotted in Fig. 2(c) at several positions just above and into the Au, and the continuous (across the boundary) 1D plot is shown in Fig. 2(d). The value of $\langle T_{yy} \rangle$ at or above the surface and at any point in free space provides the pressure on the Au surface, as is standard practice [48]. The numerical results from integration of the force density in Fig. 2(b) are identical to those from the stress tensor in Fig. 2(d).

Now we turn to forces on nanostructured material, as illustrated in Fig. 1. A numerical field solution is required to determine the average force density in (7), and we use the FEM [53]. All calculations are done in the frequency domain and with phasors. The vector electric field is determined directly and the magnetic field obtained as a secondary result. These fields are used to obtain the force density in (7), implemented in the same software environment. This force density is numerically integrated throughout the material and then normalized according to the unit-cell dimension to determine the time-average pressure in the direction normal to the structured film [$P_y = \langle P_y(t) \rangle$ N/m$^2$]. In all cases, a single plane wave is normally incident on the structured films considered with a power density of 318 MW/m$^2$ ($= 318 \times 10^6$ W/m$^2$), equivalent to a 1-mW beam having a 1-$\mu$m radius circular spot. Rounded corners with a 2-nm-radius quarter circle are used to artificially avoid field singularities. Following numerical convergence studies of the pressure, as the mesh density is increased (as the size of the triangular elements used to define the local, subdomain basis functions is reduced), a suitably small mesh size was selected for the simulation results.

The initial structured material we consider is a Au film with a periodic slot array, as shown in Fig. 3(a), where $\Lambda$ is the period, $W$ is the slot width, and $T$ is the Au thickness. A periodic boundary condition is placed at the left and right. As in all calculations, the total field is obtained as a superposition of the incident field and the scattered field, and the scattered field FEM solution uses a perfectly matched layer (PML) at the top and bottom to simulate unbounded space. The incident field is the field that exists with free space everywhere and no scattering structures. A 633-nm plane wave with **H** out of the plane ($H_z$, $E_x$) is normally incident from the top (shown by the red arrows). Referring to Fig. 3(a), the top surface is the front (in all but one situation treated, the incident field side) and the bottom surface is the back. The time-averaged $y$-directed force density in the material is formed using (7), and the collective $y$-directed pressure ($P_y$), assuming a $z$-invariant structure, is calculated by integrating the force density over the unit-cell area (in the $x$-$y$ plane) and dividing by the unit-cell width ($\Lambda$), with unit distance in the $z$ direction. With the incident field having $\mathbf{H} = \hat{\mathbf{z}} H_z$, surface plasmon modes are excited at the metal-vacuum interfaces (MI modes), and an MIM mode exists in the slot [20]. Fixing the slot width ($W$) at 60 nm and varying $\Lambda$ yields the transverse resonance condition for the top surface and bottom surface plasmon modes (at the Au-vacuum interfaces). The resonant condition is found to be $\Lambda = 620$ nm, which is close to the plasmon surface wave wavelength [54]. Fixing both $W$ (60 nm) and $\Lambda$ (620 nm), and

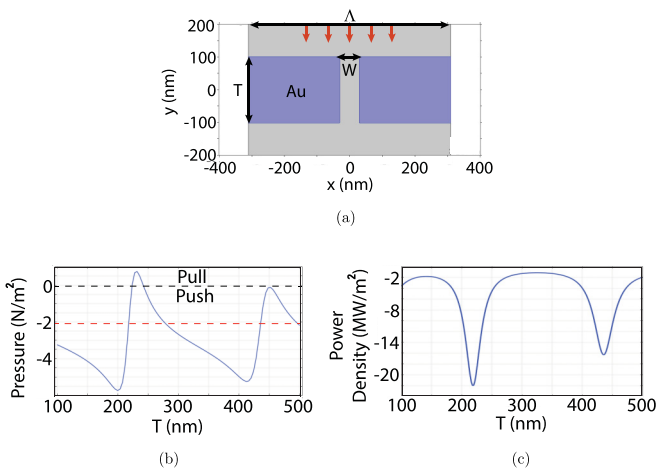


FIG. 3. Simulation of the pressure on a periodic nanoslotted Au film with plane-wave illumination and a wavelength of 633 nm. (a) Geometry with parameters: period $\Lambda$, slot width $W = 60$ nm, and Au thickness $T$. The plane wave with **H** out of plane is incident from the top (front), and the intensity is equivalent to 1 mW over a 1-$\mu$m radius circle. (b) Calculated time-averaged $y$-directed pressure with $\Lambda = 620$ nm, and $T$ varying from 100 to 500 nm. The dashed red line indicates the pressure on a perfect mirror with the same intensity, and the dashed black line is zero pressure. The region above the dashed black line is pulling and that below is pushing, because the incident plane wave is in the $-y$ direction. (c) Calculated time-averaged $y$-directed power density on the bottom (back) side of the Au membrane with respect to $T$, determined by $\Lambda^{-1}\int_\Lambda \langle S_y(x)\rangle dx$.

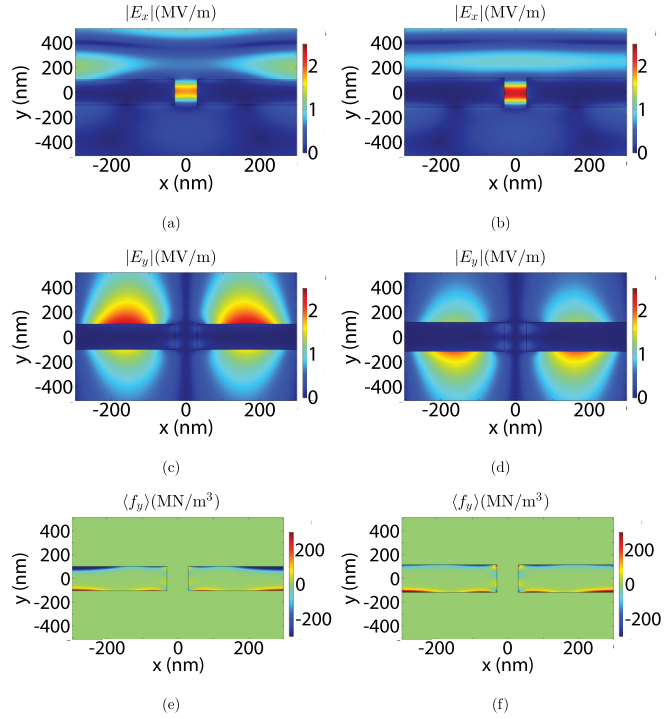


FIG. 4. The magnitude of the electric field components and the time-averaged $y$-directed force density for the largest pushing pressure case [(a), (c), and (e)], with $T = 203$ nm, and the largest pulling pressure [(b), (d), and (f)], with $T = 232$ nm, from Fig. 3(b).

varying the film thickness ($T$), we find the pressure varies as in Fig. 3(b), and has positive and negative values. The dashed black line is zero pressure and positive pressures indicate pulling because the plane wave is incident from the top and in the $-y$ direction. Figure 3(c) plots the calculated $y$-directed power density on the back side of the Au membrane with respect to $T$ [determined from $\Lambda^{-1}\int_\Lambda S_y(x)dx$ in free space and below the Au film], showing the resonant coupling features associated with the slot MIM mode. Comparing Figs. 3(b) and 3(c), we see that a pulling pressure is promoted when the power coupled to the back side of the Au membrane is near its largest magnitude. The resonances in Figs. 3(b) and 3(c) are separated by half a wavelength for the lowest-order MIM mode, corresponding to resonant coupling through that waveguide mode. The key point is that effective excitation of the back surface wave is associated with coupling light through the structure, and this results in a net pulling force, in the direction opposite to that of the incident light.

Figures 4(a), 4(c), and 4(e) show the spatial distributions of the electric field component magnitudes and the relevant force density distribution, respectively, for the largest pushing pressure case in Fig. 3(b), with $-5.77$ N/m$^2$ ($T = 203$ nm), and Figs. 4(b), 4(d), and 4(f) those for the largest pulling pressure, 0.77 N/m$^2$ ($T = 232$ nm). The dominant electric field magnitude for the slot MIM mode is $|E_x|$, shown in Figs. 4(a) and 4(b), making clear the resonance situation in Fig. 4(b) and for $T = 232$ nm that aids establishing the surface wave resonance on the back and hence pulling. The plots for $|E_y|$ in Figs. 4(c) and 4(d) highlight the MI surface wave resonances on the top (front) and bottom (back) Au-vacuum interfaces. These figures indicate more energy in the top surface wave in Fig. 4(c) for $T = 203$ nm, leading to the large pushing pressure shown in Fig. 3(b), and the enhanced bottom surface wave in Fig. 4(d) and the pulling pressure for $T = 232$ nm in Fig. 3(b). The $y$ component of the time-average force density [$\langle f_y(\mathbf{r}, t)\rangle$] is shown in Figs. 4(e) and 4(f), where blue is a pushing force density and red is a pulling force density, and these confirm the contribution of the top and bottom surface waves to the net pressure. The MIM slot mode facilities coupling to the back of the Au film, and the MI mode on the back provides pulling. From these two cases ($T = 203$ and 232 nm), it is clear that the surface waves on the top and the bottom of the Au film compete with each other and therefore decrease the magnitude of the collective pressure. We therefore conclude that the pressure could be increased if the top (for pushing) or the bottom (for pulling) surface wave is enhanced relative to that on the other side. For reference, the field magnitudes and force density for the $T = 140$ nm case from Fig. 3 are shown in Fig. 5, making clear that a weaker surface wave resonance is excited because the slot is not resonant, and this modest excitation of the top surface wave resonance results in a total (pushing) pressure of $-3.8$ N/m$^2$. As a reference, the pressure on a perfect mirror with this incident power density (318 MW/m$^2$) is $2S_i/c = -2.12$ N/m$^2$ [the red dashed line in Fig. 3(b)]. We also thus learn that excitation of surface wave resonances can lead to a pressure greater than that on a perfect mirror, and by regulating a transverse resonance condition, either pushing or pulling is achieved.

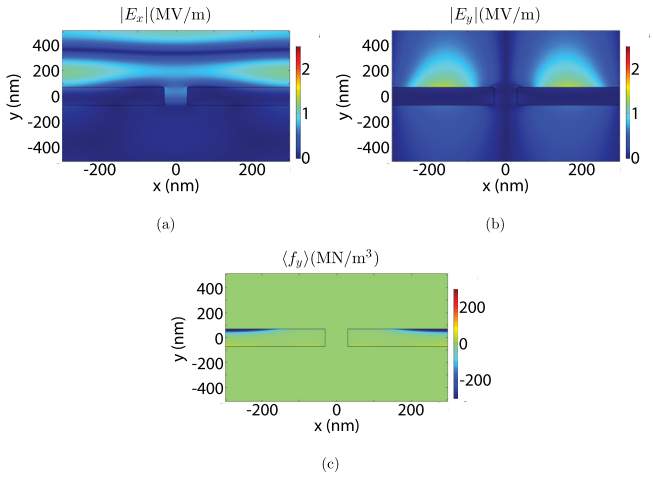


FIG. 5. The field solution and force density when $T = 140$ nm, from Fig. 3, away from the slot cavity MIM mode resonance: (a) $|E_x|$, (b) $|E_y|$, and (c) $\langle f_y \rangle$. Without the effective excitation of the MIM mode in (a), the top and bottom surface wave enhancement in (b) and hence the force density in (c) are reduced. A modest excitation of top surface wave results in collective pushing pressure of $-3.8$ N/m$^2$.

One approach to regulate the surface wave is to modify the resonance condition through control of the surface plasmon mode phase constant by adding a dielectric film. This adds a practical aspect because experiments and applications may involve membranes, and earlier optical deflection experiments used silicon nitride (SiN) membranes [27]. Figure 6(a) shows an arrangement with a SiN film (50 nm thick, $\epsilon_{\rm SiN} = 4$) on top of Au of variable thickness $T$, and where the intent here with illumination from the top with a vacuum wavelength of 633 nm is to enhance the pushing pressure. The modified wavelength of the top MI surface wave will depend on the thickness of the SiN layer. By adjusting $\Lambda$ and $T$, we find an enhanced pushing pressure of $-20.3$ N/m$^2$, with $\Lambda = 418$ nm and $T = 304$ nm (and fixed $W = 60$ nm). This occurs with a resonant top surface wave that is excited due to scatter associated with the slot, as is clear in the electric fields and force density in Figs. 6(b)–6(d). By suppressing the bottom surface wave and the pulling force density (because the MI mode at the back is not on resonance), and with contribution from the SiN layer, the pushing pressure magnitude is enhanced beyond that for a single Au layer membrane in Fig. 3. The integral of the force density in SiN and Au allows decomposition of the contributions: $-0.8$ N/m$^2$ (pushing) in the SiN film and $-19.5$ N/m$^2$ in the Au. Use of (21) and the internal boundaries in Fig. 6(e) produce a similar pressure.

By placing the 50-nm SiN film on the bottom of the Au layer, as in Fig. 7(a), we show that more effective pulling is possible. Again fixing $W = 60$ nm and scanning $\Lambda$ and $T$, we find an enhanced pulling pressure of 10.22 N/m$^2$ for $\Lambda = 420$ nm and $T = 320$ nm, leading to the results of Figs. 7(b)–7(d). Now the resonant MIM mode in the slot [Fig. 7(b)] promotes the surface wave mode on the back [Au/SiN/vacuum region, as shown in Fig. 7(c)] and a large force density on the back [Fig. 7(d)] that is dominated by the pulling force density (red), producing a net pulling pressure. In this case, the surface wave on the top has been suppressed.

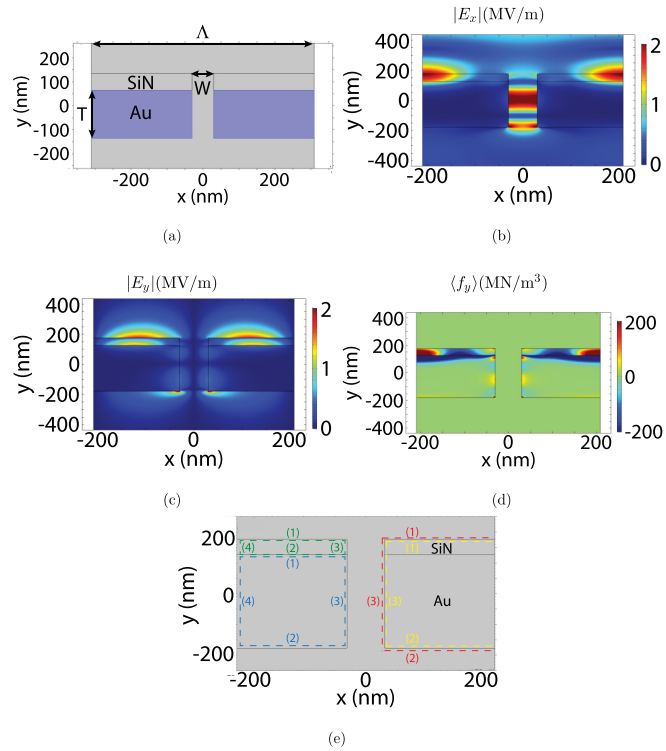


FIG. 6. The field solution and force density for an enhanced pushing pressure ($-20.3$ N/m$^2$) by adding a 50-nm SiN layer ($\epsilon_{\rm SiN} = 4$) to the top (front) of a Au film. (a) Parameters: 633-nm incident plane wave from the top (intensity equivalent to 1 mW over 1-$\mu$m radius circle), $\Lambda = 418$ nm, $W = 60$ nm, and $T = 304$ nm. (b) $|E_x|$ and (c) $|E_y|$. (d) Time-averaged $y$-directed force density. (e) Boundaries used to form the integral of the stress tensor, assuming application of the divergence theorem. The dashed line indicates the region of surface integration. Note that the dashed lines are placed only on one-half of the structure in the figure, but the corresponding pressure is calculated on both halves of the structure (the entire structure). We calculate the time-averaged pressure using $T_{yy}(x)$ for surfaces (1) and (2), and $T_{yx}(y)$ for surfaces (3) and (4). Blue (1 nm inside Au): $-17.968$ N/m$^2$. Green (1 nm inside SiN): $-0.708$ N/m$^2$. Red (1 nm outside Au and SiN): $-1.166$ N/m$^2$. Yellow (1 nm inside Au and SiN): $-1.192$ N/m$^2$. The sum of the calculated pressures from the blue- and green-dashed boundaries is very close to that determined from the force density result in (d), while the calculated pressure from the yellow-dashed boundary differs. The calculated pressure from the red-dashed boundary is very similar to that obtained by applying (22).

Note also the regions of positive and negative force density along the slot in Fig. 7(d). As in the pushing case of Fig. 6, energy is coupled into the Au/SiN/vacuum (MI) surface wave, but in Fig. 7 this is predominantly on the back. The calculated pulling pressure in SiN is 2.06 N/m$^2$ and in Au is 8.16 N/m$^2$. The enhanced total pulling pressure magnitude for the case in Fig. 7 (10.22 N/m$^2$) is less than the pushing pressure of Fig. 6 ($-20.3$ N/m$^2$). We attribute this lower magnitude to the influence of the degrees of freedom and efficacy of coupling energy through the slot to the back of the structure.

From a separate calculation, the average of the divergence of the stress tensor in the material was used, as given in (16), and that result for the force density is shown in Fig. 7(e). In

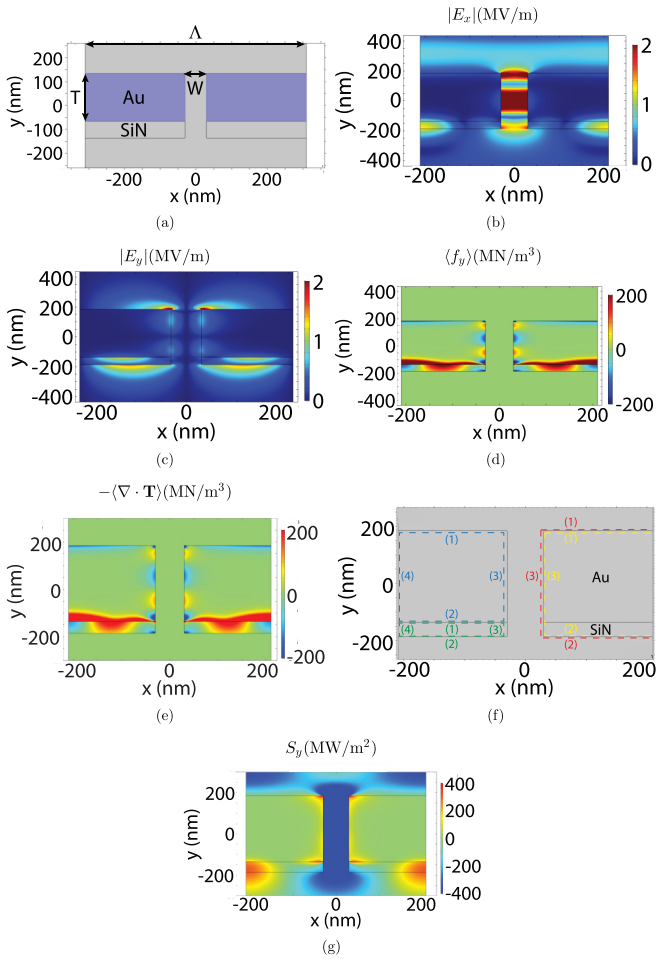


FIG. 7. The field solution and force density with an enhanced pulling pressure (10.22 N/m$^2$) from a periodic slot array in a Au film having a 50-nm SiN layer ($\epsilon_{\text{SiN}} = 4$) on the bottom (back). (a) Parameters: 633-nm incident plane wave from the front (intensity equivalent to 1 mW over 1-$\mu$m radius circle), $\Lambda = 420$ nm, $W = 60$ nm, and $T = 320$ nm. (b) $|E_x|$ and (c) $|E_y|$. (d) Time-averaged $y$-directed force density. (e) The $y$ component of the force density determined from the time-averaged divergence of the stress tensor in (16), yielding a pressure of 10.31 N/m$^2$. (f) Indication of the boundaries used to form the surface integral of the stress tensor. The dashed line indicates the region of surface integration. The average pressure is calculated using $T_{yy}(x)$ for surfaces (1) and (2), and $T_{yx}(y)$ for surfaces (3) and (4). Note that the dashed lines are placed only on one-half of the structure in the figure, the corresponding pressure is calculated on both halves of the structure (the entire structure). Blue (1 nm inside Au): 7.904 N/m$^2$. Green (1 nm inside SiN): 1.98 N/m$^2$. Red (1 nm outside Au and SiN): $-0.97$ N/m$^2$. Yellow (1 nm inside Au and SiN): $-1.918$ N/m$^2$. The sum of the calculated pressures from the blue- and green-dashed regions is very similar to the pressure calculated from the force density in (d), while the calculated pressure from the yellow-dashed region is different. The calculated pressure from red-dashed regions is very similar to the result from (22). (g) The $y$-directed power density, where the red region indicates positive values and in the direction opposite to the Poynting vector associated with the incident plane wave.

this case, the pressure obtained is 10.31 N/m$^2$. This result differs slightly from that determined using the result in Fig. 7(d), where the force density in (7) is integrated [Fig. 7(d)], only

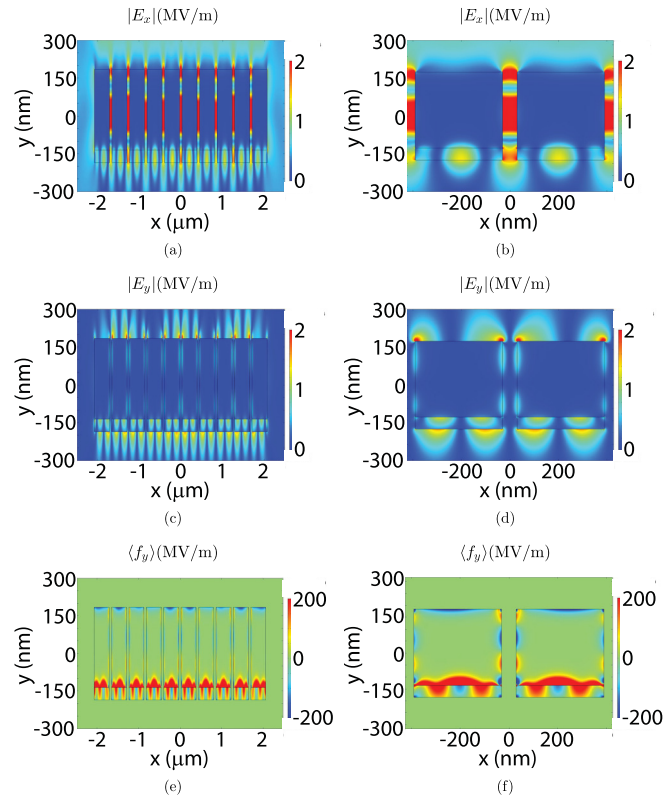


FIG. 8. The magnitude of the electric field components and the time-averaged $y$-directed force density for a finite-width structure having the same unit-cell parameters as the periodic pulling pressure case in Fig. 7. Parameters: 10 unit cells; scattered field solution with a PML on the top, bottom, left, and right; 633-nm plane wave ($H_z$, $E_x$) normally incident from the top; and an incident power density equivalent to 1 mW over 1-$\mu$m radius circle. Simulated: (a) $|E_x|$; (b) $|E_x|$ near the center of the structure; (c) $|E_y|$; (d) $|E_y|$ near the center; (e) $\langle f_y \rangle$; and (f) $\langle f_y \rangle$ near the center. The calculated pressure is 10.55 N/m$^2$, obtained by integrating the force density and then divided by the full width of the structure.

because of numerical precision. In both cases, very dense meshes have been used, in the neighborhood of $\lambda_0/600$, where $\lambda_0$ is the free-space wavelength, 633 nm in this case. While use of (7) is preferable from a computational perspective, the agreement with the independent calculations in Figs. 7(d) and 7(e) is notable. Similar results are obtained from the use of (21) and with the internal boundaries in Fig. 7(f).

Figure 8 shows simulated results for a finite number of unit cells and with the same unit-cell parameters (material arrangement and dimensions) as for Fig. 7, which assumed a periodic structure (transverse periodic boundary conditions) and that exhibited pulling [noted by the predominance of a pulling force density near the bottom and at the back in Fig. 7(d)]. There are 10 unit cells, and in the scattered field solution, a PML is used on all boundaries (top, bottom, left, and right), simulating unbounded space. A plane wave having $H_z$ is again normally incident from the top with a wavelength of 633 nm and an intensity equivalent to 1 mW over 1 $\mu$m radius spot. The structure size of 10 unit cells is representative of what might be achieved in an experiment with a Gaussian beam. Figures 8(a) and 8(b) show $|E_x|$, Figs. 8(c) and 8(d)

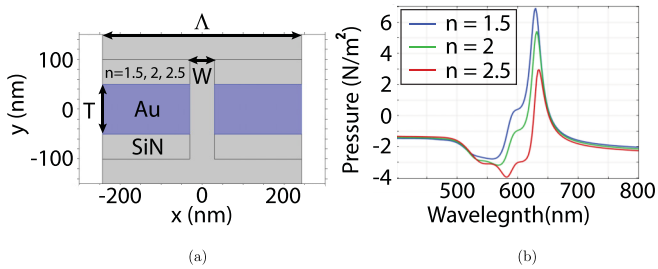


FIG. 9. Calculated wavelength-dependent pressure for a dielectric-clad Au membrane with a slot showing pushing (negative pressure) and pulling (positive pressure), depending on wavelength. (a) Geometry with 40-nm SiN (refractive index $n = 2$ at 633 nm, approximated as constant over the wavelength range used) on the bottom (back) and a 10-nm dielectric with three different refractive indices on the top (front): $n = 1.5, 2, 2.5$. A plane wave is normally incident from the top (front) with an intensity corresponding to 1 mW over 1-$\mu$m radius circle. (b) Calculated pressure: $n = 1.5$ (blue curve), $n = 2$ (green curve), and $n = 2.5$ (red curve) with $T = 306$ nm, $\Lambda = 460$ nm, and $W = 60$ nm.

$|E_y|$, and Figs. 8(e) and 8(f) the relevant component of the time-averaged force density $\langle f_y \rangle$. Figures 8(b), 8(d), and 8(f) provide an expanded scale along the $x$ direction to more easily compare the local solutions with those for the periodic case in Fig. 7. The $|E_x|$ plots make the MIM slot mode clear. Likewise, the results for $|E_y|$ demonstrate the MI-based lateral surface waves at the top and bottom, with the fields at the bottom (back) being more pronounced. As expected, away from the ends of the finite structure, all figures show results that are very close to their periodic case counterparts. The calculated pulling pressure, obtained by integrating the force density in the material and then dividing by the full width of the structure, is 10.55 N/m$^2$, which is very similar to the value from the periodic arrangement in Fig. 7 (10.22 N/m$^2$). Figure 8(c) shows two interesting features for $|E_y|$ at the top of the structure, the obvious short-length-scale magnitude variation corresponding the MI surface plasmon wavelength [as evident in Fig. 7(c)], but also a longer-length-scale beat, presenting about three periods and hence representative of a mode with a wavelength of approximately two periods of this larger-scale standing wave. This appears to be a chain waveguide mode, along the lines treated previously in relation to plasmon particle waveguides [21]. The effective wavelength for this mode presumably depends on the slot width, in addition to the metal parameters (Au at 633 nm). Our conclusion from these results for a finite-width structure is that pulling is also displayed in a manner consistent with the periodic structure. As the number of periods reduces, the field solution and the net force will of course change.

Consider now the situation where the incident wavelength is varied, and the possibility of pushing or pulling, depending on wavelength of the incident plane wave. Figure 9(a) shows a Au film with a 10-nm dielectric layer of variable refractive index ($n = \sqrt{\epsilon} = 1.5, 2, 2.5$) on the top and a 40-nm SiN layer on the bottom. The differing films on the top and bottom produce different MI surface wave wavelengths at a given free-space wavelength, allowing each to be in the vicinity of a resonance at different free-space wavelengths. We find interesting results when the Au thickness ($T$) is 306 nm and the period ($\Lambda$) is 460 nm, and the wavelength-dependent pressure calculated is shown in Fig. 9(b). The refractive index of both dielectric films is assumed independent of wavelength in this example. The wavelength-dependent dielectric constant of Au is used [52]. In Fig. 9(b), all three top dielectric film refractive indices result in both positive and negative pressures, depending on wavelength, including the SiN case ($n = 2$). For SiN film on top (green curve), the pushing pressure is $-3$ N/m$^2$ around 570 nm and the pulling pressure is 6 N/m$^2$ at 630 nm. The magnitude of the largest pushing and pulling pressure and the corresponding wavelength can be adjusted by changing the refractive index of the top dielectric layer, as Fig. 9(b) indicates: $n = 1.5$ results in the largest pulling pressure (blue, about 8 N/m$^2$) and a smaller pushing pressure (about $-2$ N/m$^2$); $n = 2.5$ and the red curve exhibit a balanced magnitude between maximum pushing and pulling pressure, around 4 N/m$^2$. There are of course other ways to vary the degrees of freedom in such a three-layer system.

The magnitudes of the calculated pressures warrant comment. At the macroscopic material level, the optical pressure on a planar surface in free space has been described by (22) [2,3]. This yields a maximum pressure (for a plane wave) of $2S/c$ N/m$^2$, a result that is consistent with (7) for a plane wave normally incident on a planar mirror (and a planar Au film and a wavelength of 633 nm produces a result just slightly lower). This perfect mirror case ($2S/c$) involves a net photon momentum exchange of $2\hbar k_0$. However, with structured media and the establishment of resonant optical fields, it has been shown to be possible to exceed this pressure [27,36] by exploiting the dimension normal to the mirrored surface and by virtue of mode resonance. This can be understood as an asymmetric cavity effect [19], where the stored photon energy increases the differential force on the two mirrors. In the results presented here, there are cavity resonances associated with surface plasmon modes, and these allow regulation of both the magnitude and direction of the total force. The dashed red line in Fig. 3(b) shows the pressure on a perfect mirror illuminated by a plane wave with the time-average power density used for these calculations. The nanostructured material and the resonances established can produce pulling and pushing pressures that are greater than for a perfect mirror. This is the case for the pushing pressure of Fig. 6, the pulling pressure of Fig. 7, and the peak pressures in Fig. 9(b). The influence of the surface waves and the establishment of resonances on the force is considered further in Sec. VI.

## VI. PULLING OF A STRUCTURE WITH AN INCIDENT PLANE WAVE

All of the simulation results presented involve sinusoidal steady-state conditions, so the fields in and surrounding the structures are established over infinite time. In practice, the time required to approximately create these conditions is on the order of the cavity lifetime. This is sufficiently short that we anticipate negligible motion of any portion of the material during this optical excitation period under modest flux rate conditions that are representative of an experimental situation. Regardless, in the situations considered, the structures have a fixed spatial arrangement for the calculation of the fields and hence the force. In an experiment and upon deflection, the

microscopic and macroscopic geometry (including the object position) will change according to various issues pertaining to the optical and mechanical properties of the structures involved.

The idea of large energy and force from a resonant system or reservoir is not new. During our history, there have been extensive studies of pendulums (by a number of scientific luminaries), and these were key in time keeping and hence of substantial importance. Instead of inserting energy after many periods (as in winding up a clock), a small external force could be applied coherently each period and at the top of the swing, where the potential energy is the maximum and the kinetic energy is zero. At the bottom of the swing, the kinetic energy can be much greater than the energy externally imparted coherently each cycle to maintain motion. There is thus much more energy in the resonant system than externally added in each cycle, and this translates to a large force that could be imparted at the bottom of the cycle in either direction, where the kinetic energy is a maximum. This is analogous to the situation with a flux of photons incident in Fig. 1 and there being many more in the transverse resonant modes associated with the surface plasmon modes. The optical cavity forms a reservoir of photons, where the energy and force is associated with the reservoir, and is not bound by the steady stream of incident photons. Such a reservoir of energy to be tapped exists in an internal combustion engine in a car that is idling with an external fuel line having a small flow of the appropriate petroleum product from another storage vessel, just enough to maintain the tank level. When the driver decides to engage the drive train and accelerate (let us forget about the refilling fuel line), the energy per unit time available to propel the car far exceeds that being input (for a while). Here, the petroleum drip is analogous to the incident photon flux and the car tank the resonant optical mode populated with photons.

Next, we reinforce the conceptual picture of how the structure depicted in Fig. 1 can be pulled by a plane wave. Periodicity results in zero net force parallel to the metal surface (the other direction where there is a component of the Poynting vector), leaving the normal component of the force to push or pull. The primary pushing and pulling described through the results in Sec. V are associated with the MI surface wave and enhanced by the presence of the dielectric film. The MI surface waves have significant energy content near to the surface (in free space and in the material). These modes propagate and resonate parallel to the metal surface, are evanescent into free space, and have a component of the real part of the time-average Poynting vector into the metal. When a transverse resonance has been established with some appreciable quality factor ($Q$) that is proportional to the cavity lifetime, the resonant fields associated with the MI plasmon have a concomitant number of photons transferring momentum per unit time to the material that is large relative to the photons in the incident plane wave. The situation of primary interest here is when the resonance is strong on the bottom (back) and diminished on the top (front). Photons in this state impart a force primarily in the upward direction, characteristic of a surface plasmon mode where the force transverse to their propagation direction is into the metal (and of course there is a component of the Poynting vector into the metal accounting for the dissipative loss). For the periodic

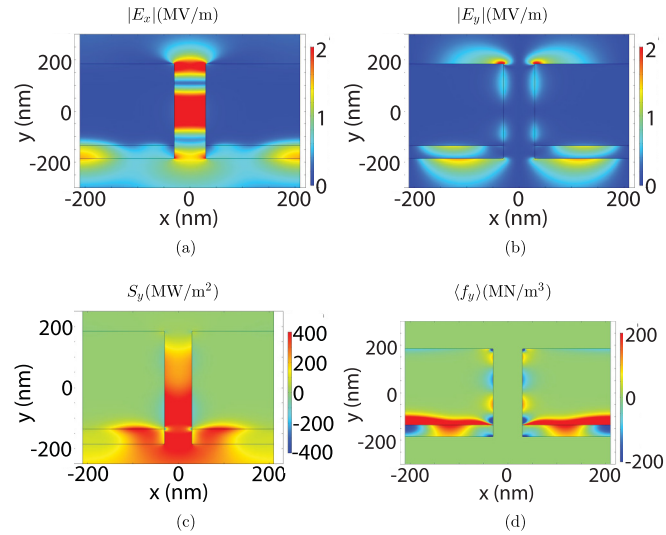


FIG. 10. The structure used in Fig. 7 is again considered, but with a plane wave incident from the bottom: 633-nm incident plane wave ($E_x$, $H_z$), with an intensity equivalent to 1 mW over 1-$\mu$m radius circle, $\Lambda = 420$ nm, $W = 60$ nm, and $T = 320$ nm. (a) $|E_x|$, showing the slot mode. (b) $|E_y|$, indicating the surface wave on the bottom and in the neighborhood of the Au-SiN interface. (c) The time-averaged $y$-directed Poynting vector component. (d) The force density determined from (7) showing a large pushing force contribution from the Au-SiN region that it similar in character to the pulling (incident field from the top) situation in Fig. 7(d).

structure considered (in the transverse direction) and the 2D field situation, this results in a net upward force and pressure, where the direct pressure from the incident flux of photons is less than from the resonant state. It is thus a resonant cavity mode excited by virtue of a resonant MIM slot mode that enables pulling.

To illustrate the influence of the surface wave, we consider the pulling case of Fig. 7, again using (7), but instead with a plane wave incident from the bottom. In the pulling situation of Fig. 7, a plane wave is normally incident from the top (Au side) and the dominant force density is near the bottom and the SiN-Au region. This results in pulling and a positive pressure because the light is incident in the $-y$ direction in this case. Consider now that same geometry, as shown in Fig. 7, but with the plane wave with the same intensity incident from the bottom (in the $+y$ direction). The calculated results are presented in Fig. 10. Figures 10(a) and 10(b) show the electric field magnitudes, making clear the slot mode (from $|E_x|$) and the surface wave (from $|E_y|$) at the bottom (Au-SiN region). Figure 10(c) shows the $y$ component of the time-average Poynting vector, with substantial positive amplitudes in the slot and the Au-SiN region at the bottom, and suggestive of a pushing force density. The resulting force density, determined from (7), is shown in Fig. 10(d). The force density is large on the incident (bottom) side and in the Au-SiN region. This results in pushing and hence a positive pressure. In this situation, there is less impact of the surface wave on the top, which is excited through the slot. This example is shown to illustrate the point that excitation of the surface wave on the bottom produces a dominant positive force density there and hence a

positive $y$-directed pressure. With illumination from the top, as in Fig. 7, force density near the bottom produces pulling.

For the planar Au film in Figs. 2(a) and 2(b), the Poynting vector indicates the direction of the force density and pressure. We now consider the local Poynting vector for the pulling structure of Fig. 7. The calculated $y$ component of the time-averaged Poynting vector $[S_y(x, y) = -1/2\,\mathrm{Re}\{E_x H_z^*\}]$ is given in Fig. 7(g). Note the relatively large negative ($-y$-directed and dark blue) values in the slot region and, importantly, the positive ($y$-directed and red) region associated with the MI surface plasmon mode at the bottom. The positive (red) Poynting vector region describes photons that are responsible for providing a pulling force on the structure. With a period of $\Lambda = 420$ nm, there is only one diffraction order that propagates in free space, that with $k_x = 0$. From the separation equation, $k_y = \sqrt{k_0^2 - (2m\pi/\Lambda)^2}$, and all plane-wave components except $m = 0$ are evanescent. In the far field, the phase fronts are thus planar and the real part of the time-average Poynting vector is independent of position. However, in the near field, where the total field involves the infinite Fourier spectrum and the contribution of the evanescent fields, the Poynting vector varies with position, as at the top of the structure in Fig. 7(g). Integrating this Poynting vector over $x$ with a fixed $y$ value, and normalizing by the period, provides the power divided by the period, hence a density. The transmitted power density can be obtained from the total fields (incident plus scattered). Use of the incident fields gives the incident power density, and with the scattered fields above the structure, the scattered power density can be formed (separate from the total power flow and possible because the background medium is lossless). The respective power densities, integrated along $x$ and then divided by $\Lambda$, yield $S_i = -3.18 \times 10^8$ W/m$^2$ (incident); $S_r = 7.07 \times 10^7$ W/m$^2$ (reflected); $S_t = -8.08 \times 10^7$ W/m$^2$ (transmitted). The calculated dissipated power density $S_d$ is $1.67 \times 10^8$ W/m$^2$. The signs correspond to the unit-vector cross products in forming the Poynting vector components and indicate the power flow direction with respect to the $y$ axis, and $S_i - (S_t - S_r) = -S_d$, as required for conservation of energy. An estimate of the pressure magnitude formed by the $-(|S_i| + |S_r| - |S_t|)/c = -1.03$ N/m$^2$, but this neglects the photons interacting with the material in the near field and in the resonant surface wave states.

We return to the pushing and pulling force cases considered in Figs. 6 and 7, respectively, in relation to options (i)–(iii), and interpretation of the force, along with application of the divergence theorem in Sec. IV. The normal electric field components to each boundary are discontinuous (TM fields with $H_z, E_x, E_y$), according to the dielectric constants involved, dictated by (48). The force has contributions associated with surface waves that are evanescent in the direction normal to the metal surfaces (for both the MI and MIM modes). Figures 6(e) and 7(f) show the integration boundaries used for the application of (21), where the force is found from the surface integral of the stress tensor elements. The blue and green dashed lines are just inside the Au and SiN boundaries. The sum of those integrations within locally homogeneous media, in each case (see the captions for Figs. 6 and 7), gives a pressure (the integrated result, normalized by $\Lambda$) that is very close to that obtained from the integral of the force densities (differing only because of the precise integration boundary node locations and numerical precision). This is consistent with option (i). However, an integration around the yellow dashed boundary just inside the material but encompassing the Au-SiN interface yields a different force because of the discontinuous normal component of the stress tensor across the interface due to the discontinuity of the normal electric field. With the boundary just outside the material, shown as the red dashed lines in Figs. 6(e) and 7(f), the numerical pressure stress tensor results differ from using the force density within the material from (7), but are similar to the Maxwell picture in (22), with a total pressure of $-1.03$ N/m$^2$ for the situation in Fig. 7 (also obtained by the total power flow estimate). This is the result from option (ii), where the stress tensor across the boundary is discontinuous. Moving the singularity in the force density at the material boundaries, to enforce continuity of the local stress tensor element, produces an external net stress tensor force that is equal to that from an integration of the internal force density, i.e., this is option (i). As presented in Sec. IV, this relates to the interpretation of the physical force on the material, and the pulling results of Sec. V are based on the interpretation in option (i).

We delve further into the application of (21) and the stress tensor character on various boundaries for the pushing case of Fig. 6 and the pulling situation in Fig. 7, in a manner consistent with option (ii) and where the stress tensor elements have discontinuities associated with discontinuous normal components of the electric fields at boundaries. The specific planar boundaries indicated by the dashed lines in Figs. 11(a) and 12(a) are used to investigate the spatially

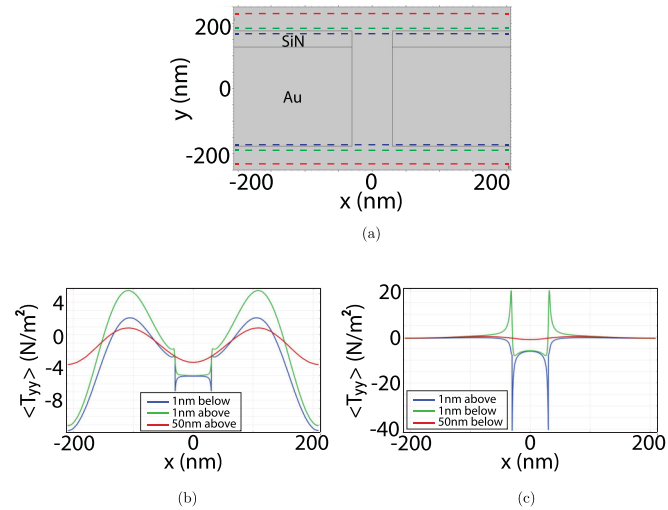


FIG. 11. The stress tensor element $\langle T_{yy}(x)\rangle$ along various surfaces for the pushing case of Fig. 6. (a) Simulation arrangement, where the dashed lines indicate the different surfaces considered for application of (21). Blue: 1 nm inside the surface; green: 1 nm outside the surface; red: 50 nm outside the surface. (b) Calculated $\langle T_{yy}(x)\rangle$ for the top three dashed lines from (a). The average pressures for those boundaries are blue: $-3.158$ N/m$^2$; green: $-1.319$ N/m$^2$; red: $-1.319$ N/m$^2$. (c) Calculated $\langle T_{yy}(x)\rangle$ for the bottom three dashed lines from (a). The pressures averaged over $x$ are 1.813 N/m$^2$ (blue); 0.156 N/m$^2$ (green); 0.156 N/m$^2$ (red).

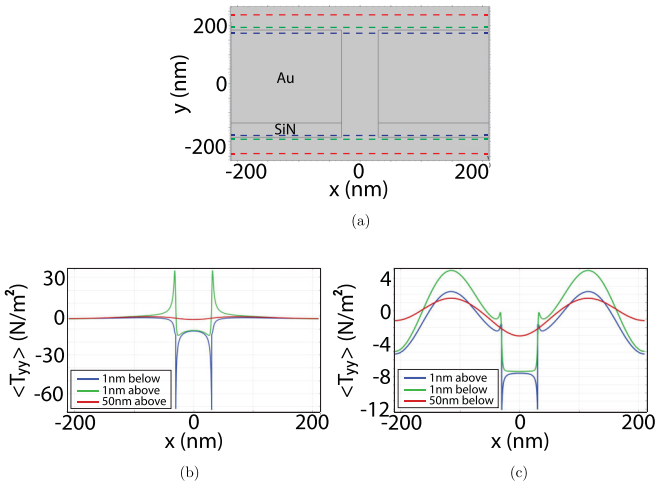


FIG. 12. The stress tensor element $\langle T_{yy}(x)\rangle$ along various surfaces for the pulling case of Fig. 7. (a) Simulation arrangement, where the dashed lines indicate the surfaces used to evaluate the stress tensor. Blue: 1 nm inside the surface; green: 1 nm outside the surface; red: 50 nm outside the surface. (b) Calculated $\langle T_{yy}(x)\rangle$ for the top three dashed lines from (a). The average pressures are $-4.148$ N/m$^2$ (blue); $-1.3$ N/m$^2$ (green); $-1.3$ N/m$^2$ (red). (c) Calculated $\langle T_{yy}(x)\rangle$ for the bottom three dashed lines from (a). The average pressures are 1.816 N/m$^2$ (blue); 0.27 N/m$^2$ (green); 0.27 N/m$^2$ (red).

dependent stress tensor for the pushing and pulling geometries, Figs. 6 and 7, respectively. For these boundaries, only $T_{yy}$ in (21) contributes. For the pushing situation in Fig. 11(b), two boundaries just above the structure and in free space (red, 50 nm above; green, 1 nm above) and one just into the SiN and spanning the slot (1 nm below the top surface, blue) are shown. Note how the local $\langle T_{yy}(x)\rangle$ changes with the $y$ position of the boundary, even above the structure and in free space, according to the near fields. However, the total surface integral result, the sum over the top and bottom surfaces, is unchanged when integrating in free space, as the free-space boundary is changed. This can be understood by the force density being zero in free space. Figure 11(c) shows the corresponding stress tensor results for the surfaces indicated near the bottom of the structure in Fig. 11(a). One obviously sees the character of the MIM slot mode in Figs. 11(b) and 11(c). However, it is interesting to note the changing sign of $\langle T_{yy}(x)\rangle$, in particular, close to the Au interface. Turning now to the pulling situation depicted in Fig. 12, the changing roles of the results for $\langle T_{yy}(x)\rangle$ for the boundaries near the top and bottom are clear. Also clear in Fig. 12(c) is the oscillating character of $\langle T_{yy}(x)\rangle$, where positive values correspond to local pulling. We thus note that use of option (ii), which is consistent with the Maxwell description in (22), provides information related to pulling.

We conclude by reiterating that the enablers for enhanced pushing or pulling are the associated MI surface wave resonances. These MI modes are excited by the slot, and when it is resonant for the MIM mode and the bottom surface wave is resonant, with the front tuned off resonance, pulling can occur. This situation is anecdotal in that other resonant arrangements will presumably behave similarly.

## VII. CONCLUSIONS

A rigorous theory for optical forces has been presented and evaluated for situations where the normal component of the electric field is discontinuous across material boundaries. Notably, this occurs for plasmonic surface waves at metal-dielectric interfaces. Using an established position where the momentum-flow (stress) tensor is continuous across boundaries, resonances in the surface plasmon modes can be regulated to provide for a pulling force. With such resonant conditions, and the evanescent nature of the surface wave that confines the fields to the metal interface, substantial energy is stored in the material, and this leads to enhanced pressure and opportunities for pulling. The pulling force from a surface wave on the bottom of the material can be understood as being due to the same physical phenomenon that leads to pushing when the surface wave is excited on the top, but with an oppositely directed force because of the nature of the fields and local force density associated with the surface wave. The results presented motivate experimental studies to investigate related optical force phenomena.

In all cases, the object is fixed in position and the electromagnetic excitation is sinusoidal steady state. In practice, there needs be an excitation time duration that is adequate to excite the resonant modes in the structure, with the object fixed in position. The effect can be understood as being based upon the wave nature of light, where the associated photons transfer momentum in a manner consistent with the asymmetric cavities formed by the respective resonant plasmon surface waves. With the establishment of a dominant plasmon surface wave on the top (front), pushing occurs, but with a dominant surface wave on the back (bottom), pulling results. Earlier concepts that allow pulling with a laser beam involved use of tweezer traps or structured beams and small particles that perturb the field. To the contrary, in our work, the scattered field is large and regulated to promote pushing or pulling, and the force is enhanced through resonances. The multilayer structured membranes simulated have a complex force density that may result in strain that in turn leads to local deformations or optical material property changes, providing an interesting dimension in optomechanics.

The understanding that field resonances in materials can be used to regulate optical forces should lead to new classes of optomechanical devices and associated application spaces. For instance, pushing and pulling of a structure, depending on wavelength, provides a new dimension in remote control. This could also be used in conjunction with photomotility to regulate the position of material and a mirror. The effect might be used in integrated optics, for instance, in a flow cytometry arrangement, or for all-optical routing of signals. New opportunities in mechanical cooling should exist based on this work. Finally, use of nanostructured material in optomechanics could be utilized for nonreciprocal elements.

## ACKNOWLEDGMENTS

This work was supported by the Air Force Office of Scientific Research (Grant No. FA9550-19-1-0259), the Army Research Office (Grant No. W911NF-16-1-0359), and the National Science Foundation (Grant No. 1927822).

## APPENDIX: SINUSOIDAL STATE TIME-AVERAGE FORCE DENSITY

For the case of sinusoidal fields [$\exp(-i\omega t)$, with a single $\omega$], we show that

$$\left\langle \frac{\partial \mathbf{g}}{\partial t} \right\rangle = 0. \tag{A1}$$

This result is utilized in forming (12).

Consider the time-averaged electromagnetic force due to monochromatic light, with $\mathbf{E}(t) = \hat{\mathbf{e}}\,\mathrm{Re}\{E\exp(-i\omega t)\}$ and $\mathbf{H}(t) = \hat{\mathbf{h}}\,\mathrm{Re}\{H\exp(-i\omega t)\}$, and $\hat{\mathbf{e}} \times \hat{\mathbf{h}} = \hat{\mathbf{s}}$. For the Abraham momentum situation, and using $E = E' + iE''$ and $H = H' + iH''$, we have

$$\begin{aligned}
\frac{\partial}{\partial t}(\mathbf{E}\times\mathbf{H}) &= \hat{\mathbf{s}}\frac{\partial}{\partial t}(\mathrm{Re}\{Ee^{-i\omega t}\}\mathrm{Re}\{He^{-i\omega t}\}) \\
&= \hat{\mathbf{s}}[\mathrm{Re}\{-i\omega(E'+iE'')(\cos\omega t - i\sin\omega t)\}\mathrm{Re}\{(H'+iH'')(\cos\omega t - i\sin\omega t)\} \\
&\quad + \mathrm{Re}\{(E'+iE'')(\cos\omega t - i\sin\omega t)\}\mathrm{Re}\{-i\omega(H'+iH'')(\cos\omega t - i\sin\omega t)\}] \\
&= \hat{\mathbf{s}}[(-\omega E'\sin\omega t + \omega E''\cos\omega t)(H'\cos\omega t + H''\sin\omega t) + (E'\cos\omega t + E''\sin\omega t) \\
&\quad \times(-\omega H'\sin\omega t + \omega H''\cos\omega t)].
\end{aligned} \tag{A2}$$

Therefore, the time average becomes

$$\left\langle \frac{\partial}{\partial t}(\mathbf{E}\times\mathbf{H}) \right\rangle = \hat{\mathbf{s}}[-\omega E'H''\langle\sin^2\omega t\rangle + \omega E''H'\langle\cos^2\omega t\rangle + \omega E'H''\langle\cos^2\omega t\rangle - \omega E''H'\langle\sin^2\omega t\rangle] = 0. \tag{A3}$$


[1] P. N. Lebedev, Ann. Phys. **6**, 433 (1901).
[2] E. F. Nichols and G. F. Hull, Phys. Rev. **17**, 26 (1903).
[3] J. C. Maxwell, *A Treatise on Electricity and Magnetism*, Vol. 2 (Dover, New York, 1954); this is an unabridged, slightly altered, republication of the third edition, published by the Clarendon Press, Oxford, in 1891.
[4] A. Ashkin and J. M. Dziedzic, Phys. Rev. Lett. **30**, 139 (1973).
[5] A. Ashkin, J. M. Dziedzic, J. E. Bjorkholm, and S. Chu, Opt. Lett. **11**, 288 (1986).
[6] J. R. Moffitt, Y. R. Chemla, S. B. Smith, and C. Bustamante, Annu. Rev. Biochem. **77**, 205 (2008).
[7] S.-H. Lee, Y. Roichman, and D. G. Grier, Opt. Express **18**, 6988 (2010).
[8] J. Chen, J. Ng, Z. Lin, and C. Chan, Nat. Photonics **5**, 531 (2011).
[9] S. Sukhov and A. Dogariu, Phys. Rev. Lett. **107**, 203602 (2011).
[10] J. Damková, L. Chvátal, J. Ježek, J. Oulehla, O. Brzobohatý, and P. Zemánek, Light Sci. Appl. **7**, 17135 (2018).
[11] K. J. Webb and M.-C. Yang, Phys. Rev. E **74**, 016601 (2006).
[12] A. Mizrahi and Y. Fainman, Opt. Lett. **35**, 3405 (2010).
[13] K. J. Webb and Shivanand, Phys. Rev. E **84**, 057602 (2011).
[14] K. J. Webb, J. Opt. Soc. Am. B **29**, 1904 (2012).
[15] M. L. Povinelli, M. Lončar, M. Ibanescu, E. J. Smythe, S. G. Johnson, F. Capasso, and J. D. Joannopoulos, Opt. Lett. **30**, 3042 (2005).
[16] M. Li, W. Pernice, and H. Tang, Nat. Photonics **3**, 464 (2009).
[17] H. Li, Y. Cao, B. Shi, T. Zhu, Y. Geng, R. Feng, L. Wang, F. Sun, Y. Shi, M. A. Miri *et al.*, Phys. Rev. Lett. **124**, 143901 (2020).
[18] J. Nemirovsky, M. C. Rechtsman, and M. Segev, Opt. Express **20**, 8907 (2012).
[19] Y.-C. Hsueh, L.-F. Yang, and K. J. Webb, Phys. Rev. B **99**, 045437 (2019).
[20] K. J. Webb and J. Li, Phys. Rev. B **73**, 033401 (2006).
[21] K. J. Webb and J. Li, Phys. Rev. B **72**, 201402(R) (2005).
[22] K. J. Webb and J. Li, Opt. Lett. **31**, 3348 (2006).
[23] A. Einstein and J. Laub, Ann. Phys. **331**, 541 (1908).
[24] M. Mansuripur, A. R. Zakharian, and E. M. Wright, Phys. Rev. A **88**, 023826 (2013).
[25] K. J. Webb, Phys. Rev. Lett. **111**, 043602 (2013).
[26] K. J. Webb, Phys. Rev. B **94**, 064203 (2016).
[27] L.-F. Yang, A. Datta, Y.-C. Hsueh, X. Xu, and K. J. Webb, Phys. Rev. Lett. **122**, 083901 (2019).
[28] G. Agarwal, D. Pattanayak, and E. Wolf, Phys. Rev. B **10**, 1447 (1974).
[29] A. Boardman, B. Paranjape, and Y. O. Nakamura, Phys. Status Solidi **75**, 347 (1976).
[30] L. Kleinman, Phys. Rev. **160**, 585 (1967).
[31] R. Resta, Phys. Rev. B **16**, 2717 (1977).
[32] Y. Luo, A. I. Fernandez-Dominguez, A. Wiener, S. A. Maier, and J. B. Pendry, Phys. Rev. Lett. **111**, 093901 (2013).
[33] C. Ciraci, J. B. Pendry, and D. R. Smith, ChemPhysChem **14**, 1109 (2013).
[34] A. Wiener, A. I. Fernández-Domínguez, A. P. Horsfield, J. B. Pendry, and S. A. Maier, Nano Lett. **12**, 3308 (2012).
[35] A. Moreau, C. Ciraci, and D. R. Smith, Phys. Rev. B **87**, 045401 (2013).
[36] A. H. Velzen and K. J. Webb, Phys. Rev. B **92**, 115416 (2015).
[37] J. P. Gordon, Phys. Rev. A **8**, 14 (1973).
[38] W. Shockley, Proc. Natl. Acad. Sci. USA **60**, 807 (1968).
[39] F. N. H. Robinson, Phys. Rep. **16**, 313 (1975).
[40] J. H. Strait, G. Holland, W. Zhu, C. Zhang, B. R. Ilic, A. Agrawal, D. Pacifici, and H. J. Lezec, Phys. Rev. Lett. **123**, 053903 (2019).
[41] D. F. Nelson and M. Lax, Phys. Rev. B **13**, 1770 (1976).
[42] H. A. Haus and H. Kogelnik, J. Opt. Soc. Am. A **66**, 320 (1976).
[43] R. N. C. Pfeifer, T. A. Nieminen, N. R. Heckenberg, and H. Rubinsztein-Dunlop, Phys. Rev. A **79**, 023813 (2009).
[44] C. Baxter and R. Loudon, J. Mod. Opt. **57**, 830 (2010).

[45] P. Penfield and H. A. Haus, *Electrodynamics of Moving Media* (MIT Press, Cambridge, MA, 1967).
[46] I. Brevik, Phys. Rep. **52**, 133 (1979).
[47] J. Schwinger, Found. Phys. **13**, 373 (1983).
[48] J. D. Jackson, *Classical Electrodynamics* (Wiley, Hoboken, NJ, 2007).
[49] P. Parashar, K. A. Milton, Y. Li, H. Day, X. Guo, S. A. Fulling, and I. Cavero-Peláez, Phys. Rev. D **97**, 125009 (2018).
[50] M. Mansuripur, Opt. Express **12**, 5375 (2004).
[51] R. V. Jones and B. Leslie, Proc. R. Soc. Lond. A **360**, 347 (1978).
[52] P. B. Johnson and R.-W. Christy, Phys. Rev. B **6**, 4370 (1972).
[53] COMSOL, COMSOL multiphysics modeling software, http://www.comsol.com.
[54] S. A. Maier, *Plasmonics: Fundamentals and Applications* (Springer, New York, 2007).